HOKKAIDO UNIVERSITY

Title	Probing the Biogenesis of Polysaccharide Granules in Algal Cells at Sub-Organellar Resolution via Raman Microscopy with Stable Isotope Labeling
Author(s)	Yonamine, Yusuke; Asai, Takuya; Suzuki, Yuta et al.
Citation	Analytical chemistry, 93(50), 16796-16803 https://doi.org/10.1021/acs.analchem.1c03216
Issue Date	2021-12-21
Doc URL	https://hdl.handle.net/2115/87586
Rights	This document is the Accepted Manuscript version of a Published Work that appeared in final form in Analytical Chemistry, copyright c American Chemical Society after peer review and technical editing by the publisher. To access the final edited and published work see https://pubs.acs.org/articlesonrequest/AOR-CPMXG7AHEMEXN7BS36SG.
Rights(URL)	https://pubs.acs.org/articlesonrequest/AOR-CPMXG7AHEMEXN7BS36SG.
Type	journal article
File Information	Main text (Revised) clean.pdf

Hokkaido University Collection of Scholarly and Academic Papers : HUSCAP

Probing the biogenesis of polysaccharide granules in algal cells at sub-organellar resolution via Raman microscopy with stable isotope labeling

Yusuke Yonamine[a*], Takuya Asai[b], Yuta Suzuki[b], Takuro Ito[c,d,e], Yasuyuki Ozeki[b*], and Yu Hoshino[f*]

[a]*Research Institute for Electronic Science, Hokkaido University, Kita21, Nishi10, Kita-ku, Sapporo 001-0021, Japan*

[b]*Department of Electrical Engineering and Information Systems, The University of Tokyo, 7-3-1 Hongo, Bunkyo-ku, Tokyo 113-8656, Japan*

[c]*Department of Chemistry, The University of Tokyo, 7-3-1 Hongo, Bunkyo-ku, Tokyo 113-0033, Japan*

[d]*Japan Science and Technology Agency, 4-1-8, Honcho, Kawaguchi, Saitama 332-0012, Japan*

[e]*Department of Creative Engineering, National Institute of Technology, Tsuruoka College, 104 Sawada, Inooka, Tsuruoka, Yamagata 997-8511, Japan*

[f]*Department of Chemical Engineering, Kyushu University, 744 Motooka, Fukuoka 819-0395, Japan*

*E-mail: yonamine@es.hokudai.ac.jp, ozeki@ee.t.u-tokyo.ac.jp, yhoshino@chem-eng.kyushu-u.ac.jp

ABSTRACT: Phototrophs assimilate CO_2 into organic compounds that accumulate in storage organelles. Elucidation of the carbon dynamics of storage organelles could enhance the production efficiency of valuable compounds and facilitate the screening of strains with high photosynthetic activity. To comprehensively elucidate the carbon dynamics of these organelles, the intra-organellar distribution of the carbon atoms that accumulate at specific time periods should be probed. In this study, the biosynthesis of polysaccharides in storage organelles was spatiotemporally probed via stimulated Raman scattering (SRS) microscopy using a stable isotope (^{13}C) as the tracking probe. Paramylon granules (a storage organelle of β-1,3-glucan) accumulated in a unicellular photosynthetic alga, *Euglena gracilis,* were investigated as a model organelle. The carbon source of the culture medium was switched from $NaH^{12}CO_3$ to $NaH^{13}CO_3$ during the production of the paramylon granules; this resulted in the distribution of the ^{12}C and ^{13}C constituents in the granules so that the biosynthetic process could be tracked. Taking advantage of high-resolution SRS imaging and label switching, the localization of the ^{12}C and ^{13}C constituents inside a single paramylon granule could be visualized in three dimensions, thus revealing the growth process of paramylon granules. We propose that this method can be used for comprehensive elucidation of the dynamic activities of storage organelles.

INTRODUCTION

Phototrophs assimilate CO_2 into carbohydrates that produce metabolites via downstream pathways. These organic compounds are stored in specific organelles, including starch granules in amyloplasts,[1–3] polysaccharide granules of β-glucans,[4,5] lipid droplets,[6,7] protein bodies,[8–10] and protein storage vacuoles.[11,12] These storage organelles undergo dynamic metabolic processes (biogenesis and degradation) and intracellular trafficking as response to the cell cycle and extracellular environments.[12–16] The distribution of the carbon atoms that accumulate at specific time periods in the organelles should be probed to comprehensively elucidate the carbon dynamics of the organelles. Elucidation of the detailed metabolic processes can enhance the production efficiency of valuable compounds, including foods,[17,18] biofuels,[19,20] and recombinant proteins.[21] Furthermore, monitoring carbon fixation affords the criteria for screening strains that exhibit high photosynthetic activities, which can contribute to the reduction in atmospheric CO_2 levels.

Conventionally, proteomic and metabolomic analyses combined with stable isotope (SI) labeling[22–24] have revealed the carbon fluxes of storage organelles. However, they only provide average metabolic information for a large population of organelles and do not provide spatial information, such as distribution and localization, in organelles; this is also not achieved through subcellular analysis of isolated organelles.[22] In addition, proteomic and metabolomic analyses are not applicable to bio-polymers with heterogeneous molecular weights such as polysaccharides. In contrast, fluorescence microscopy performed with fluorescent probes[25,26] visualizes the spatial information (shape, amount, and distribution) of storage organelles. However, fluorescence imaging exhibits several critical limitations in capturing the dynamics of storage organelles, such as the limited applicability of pulse-chase analysis,[27] perturbation of cellular metabolism by fluorescence staining,[28–30] and photobleaching, which prevents long-term monitoring.[25] Thus, spatiotemporal investigation of storage organelles remains challenging by conventional methods.

Conversely, Raman microscopy combined with SI labeling can spatiotemporally probe metabolic dynamics,[31–48] thereby offering the following significant advantages for investigating storage organelles: first, cellular metabolic processes, even in a dynamic equilibrium, can be tracked by exposing cells to SI-labeled substrates,

and the localization and distribution of the SI-labeled products in the cells can be detected by Raman microscopy.[48] Second, SI-labeled substrates do not interfere with the biological functions of cells because their physiological properties are hardly affected by SI labeling.[49] Third, SI labeling is applicable to a wide range of target biomolecules, including proteins,[32–38] DNA,[37–39] lipids,[40–43] polysaccharides,[44,45] and small metabolites,[46–48] in different cell types by selecting SI-labeled substrates that are present in the desired metabolic pathways. Fourth, because Raman microscopy is free from photobleaching, Raman imaging combined with SI labeling can be used for long-term monitoring of organelle activity.

Previously, we probed photosynthetic activity of a unicellular alga, *Euglena gracilis*,[50–52] by Raman microscopy with SI-labeled water (D_2O) as the substrate.[44] The results revealed that D_2O was assimilated and incorporated into paramylon granules (the storage organelles composed of β-1,3-glucan) through not only photosynthesis but also other enzymatic reactions, which prevented the specific probing. We then confirmed that $^{13}CO_2$, the other substrate of photosynthesis, is a specific probe of photosynthetic activity and applied it to monitor production of paramylon granules in an single *E. gracilis* cell isolated in a microfluidic chip for a long term.[45] Stimulated Raman scattering (SRS) microscopy revealed the incorporation of ^{13}C into the paramylon granules, proving the photosynthetic activity was maintained, whereas it still remains to be elucidated the detailed growing process.

In this study, we further investigated the carbon dynamics in a single paramylon granule via SRS microscopy at sub-organellar resolution and statistical image analysis including segmentation of the granule, in which $^{13}CO_2$ is exposed to different conditions as the tracking probe (Figure 1). Specifically, the carbon source of the culture medium was switched from $NaH^{12}CO_3$ to $NaH^{13}CO_3$ during production of the paramylon granules, and the distribution of the ^{12}C and ^{13}C constituents in a paramylon granule was observed to track the biosynthetic process. Owing to high-resolution SRS imaging, the localization of the ^{12}C and ^{13}C constituents inside a single paramylon granule was visualized in three dimensions (3D), which revealed the growth process of the granules. Because paramylon granules are converted into wax esters by *E. gracilis* cells,[53–55] which can be refined into biodiesel,[19,20] elucidation of the detailed metabolic process of paramylon granules could be valuable in enhancing the production efficiency of algal biofuel by capturing CO_2 from the atmosphere.

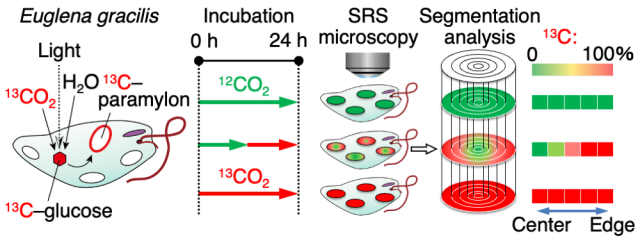

Figure 1. Schematic of our approach. The biogenesis of paramylon granules in an algal cell was investigated via SRS microscopy employing $^{13}CO_2$ and $^{12}CO_2$ substrates that were exposed to different conditions and subsequent segmentation analysis of each granule.

EXPERIMENTAL SECTION

Algal Material and Culture Conditions. *Euglena gracilis* NIES-48 was obtained from the Microbial Culture Collection at the National Institute for Environmental Studies (NIES, Tsukuba, Ibaraki, Japan). An autotrophic medium (AF-6) was employed for culturing (working volume: 20 mL). The cells were grown in culture flasks (a 50-mL polystyrene-suspension culture flask with a filter cap, Greiner Bio-One Co., Ltd., Tokyo, Japan) under static conditions of 14-hour light/10-hour dark cycle (~100 μmol/m^2s^{-1}) at 28 °C. Before inducing the growth of the paramylon granules with an SI medium, the *E. gracilis* cells were grown in a normal AF-6 medium at a pH of 6.6 for a minimum of 3 days as a preculture. In the exponential growth phase, the cells in the preculture were transferred to a nitrogen-deficient AF-6 medium (without NH_4NO_3 and $NaNO_3$) containing 20 mM ^{13}C–sodium bicarbonate ($NaH^{13}CO_3$; ^{13}C, 99%; Cambridge Isotope Laboratories, Inc., Tewksbury, MA, USA) or ^{12}C–sodium bicarbonate ($NaH^{12}CO_3$; Nacalai Tesque, Inc., Kyoto, Japan) to induce the growth of ^{13}C– or ^{12}C–paramylon granules in the culture flasks (polystyrene-suspension culture flask with a standard screw cap, 50 mL volume, Greiner Bio-One Co., Ltd., Tokyo, Japan) at a density of 1×10^5 cells mL^{-1} (working volume: 20 mL). The cells were incubated under continuous light illumination (~150 μmol/m^2s^{-1}) at 28 °C. To switch the incubation atmosphere from the ^{12}C to ^{13}C source, the cells were transferred from the nitrogen-deficient AF-6 medium with $NaH^{12}CO_3$, to that with $NaH^{13}CO_3$ for different durations (3, 6, 12, and 18 h) during the 24-hour incubation period (Figure 5a). To induce the paramylon granules containing the ^{13}C and ^{12}C constituents, the cells were incubated in a nitrogen-deficient AF-6 medium containing $NaH^{13}CO_3$ and $NaH^{12}CO_3$ at different ratios (molar ratios of $NaH^{13}CO_3$ to $NaH^{12}CO_3$ were 0:100, 25:75, 50:50, 75:25, and 100:0; final concentration of total $NaHCO_3$: 20 mM) for 5 days. Regarding the SRS microscopy analysis, the cells were immobilized using a 0.25% glutaraldehyde solution and concentrated via centrifugation (1100×*g* for 5 min).

Extraction of the ^{13}C- and ^{12}C-labeled Paramylon Granules from the *E. gracilis* Cells. The ^{13}C– and ^{12}C–paramylon granules were extracted from the *E. gracilis* cells according to a previously reported procedure.[45,56] After inducing the production of paramylon granules, an aliquot (1.5×10^7 cells) was collected and resuspended in 1.8 mL of deionized water and subsequently mixed with 0.2 mL of ice-cold 30% perchloric acid. The mixture was vortexed for 1 min before it was centrifuged for 2 min at 1100×*g*. The supernatant was discarded, 2 mL of 1% sodium dodecyl sulfate was added to the pellet, and the mixture was vortexed for 1 min before it was heated in boiling water for 15 min. Thereafter, the sample was centrifuged for 5 min at 1100×*g*, and the supernatant was discarded; these steps were repeated two times. The resulting pellets were freeze-dried and analyzed via SRS microscopy.

SRS Imaging of the ^{13}C- and ^{12}C-Labeled *E. gracilis* Cells. SRS imaging of the *E. gracilis* cells was conducted in a manner similar to that reported previously.[57–59] For 2D imaging including Figure 2–4, 5b, and 5d, hyperspectral SRS images at 91 spectral points between 2800 and 3100 cm^{-1} (at intervals of 3.3 cm^{-1}) were acquired successively. The spectral resolution of the SRS microscope was ~5 cm^{-1}. For 3D SRS imaging including Figure 5e and 5f, the following procedures were modified: the SRS data were acquired at seven spectral points (2860, 2880, 2896, 2910, 2925, 2937, and 3050 cm^{-1}) to accelerate the scanning speed compared with that of hyperspectral data. The number of pixels of the Raman image was 500 × 500 pixels for a field of view of 80 μm × 80 μm at a mapping speed of 30 frames per second (0.033 s per image). Accordingly, only 0.23 s was required to obtain one cross-sectional 2D image by considering one accumulation as one scan. The stage position was scanned with a 0.5-micrometer step along the depth direction to obtain a total of 20 cross-sectional images.

To discriminate spatial distributions of three constituents (^{13}C– and ^{12}C–paramylon granules as well as the chloroplasts), the SRS data $\mathbf{d}_j$ at the j^{th} pixel were decomposed using the spectral bases $\mathbf{s}_i$ acquired from the three pure constituents ($\mathbf{s}_1$, ^{13}C–paramylon granules; $\mathbf{s}_2$, ^{12}C–paramylon granules; $\mathbf{s}_3$, chloroplasts), that is, $\mathbf{d}_j = c_{j1}\mathbf{s}_1 + c_{j2}\mathbf{s}_2 + c_{j3}\mathbf{s}_3$, where the coefficients c_{ji} are the concentrations of the corresponding constituents. The spectral bases of the

hyperspectral (91 points, Figure S8a) and multispectral (7 points, Figure S9a) SRS data were employed to obtain the pseudo-inverse matrices, respectively (Figure S8b and S9b). We used them to obtain the spatial distributions of the three constituents from each SRS image of *E. gracilis* cells as 2D images. To obtain a 3D SRS image, the cross-sectional 2D images were stacked by the ImageJ software.[60,61]

Statistical Analyses of the SRS Images for the ^{13}C Ratios of the Paramylon Granules. The ^{13}C ratios of the paramylon granules containing the ^{13}C and ^{12}C constituents were analyzed from their SRS images employing the CellProfiler software.[62] The software was employed to plot the histograms, heatmaps, and averages with standard deviations of the ^{13}C ratios (Figure S1). First, the SRS images of the extracted paramylon granules or *E. gracilis* cells, in which the granules were accumulated, were split into three channels (^{13}C– and ^{12}C–paramylon granules as well as the chloroplasts) based on their respective spectral bases. The split images of the ^{13}C– and ^{12}C–paramylon constituents were stacked and merged to obtain the total intensities of both signals. The merged image was converted into a mask of paramylon granules with threshold sizes (a mask for each whole granule). The each granule mask was further segmented into five regions from the center to the periphery for analyzing localization of ^{13}C– and ^{12}C–paramylon constituents. The resultant masks were applied to the original SRS images (^{13}C– or ^{12}C–paramylon constituents) to obtain the total intensity in each paramylon-granule-masked area. The intensities of the ^{13}C– and ^{12}C–paramylon constituents were employed to calculate the ^{13}C ratios and plot the graphs.

RESULTS AND DISCUSSION

SRS Imaging of the *E. gracilis* Cells Accumulating the ^{13}C– or ^{12}C–Paramylon Granules. First, the *E. gracilis* cells accumulating the ^{13}C– and ^{12}C–paramylon granules were differentiated by SRS imaging based on the shift in the Raman spectra. The production of the paramylon granules was induced in the cells for 24 h using culture media containing ^{13}C– and ^{12}C–$NaHCO_3$ as the $^{13}CO_2$ and $^{12}CO_2$ sources, respectively. The Raman spectra of the three constituents (^{13}C– and ^{12}C–paramylon granules as well as the chloroplasts) were identified, and a redshift was observed in the spectrum of the ^{13}C–paramylon granules compared with the ^{12}C–paramylon granules (shift in the peak, 13 cm^{-1}; Figure 2a) in the CH stretching region (2800–3100 cm^{-1}). This result demonstrated that $^{13}CO_2$ was incorporated into the *E. gracilis* cells and converted subsequently into paramylon granules through carbon fixation. Further, the *E. gracilis* cells that accumulated the ^{13}C– or ^{12}C–paramylon granules were differentiated by SRS imaging. The Raman spectra of the three constituents of the *E. gracilis* cells (Figure 2a) were employed for the linear decomposition, after which the ^{13}C– and ^{12}C–paramylon granules as well as the chloroplasts were color-coded as red, green, and blue, respectively, to acquire tricolor Raman images in the RGB color model.[58] SRS imaging clearly differentiated the two types of cells accumulating the ^{13}C– or ^{12}C–paramylon granules (Figure 2b). These results indicate that $^{13}CO_2$ was converted into ^{13}C–paramylon granules through cellular metabolism, and the Raman spectrum of the CH stretching region revealed a red-shift through which SRS imaging clearly discriminated the ^{13}C– and ^{12}C–paramylon granules.

SRS Imaging of the Paramylon Granules that were Incubated by a Mixture of the ^{13}C and ^{12}C Sources. Second, the Raman spectral shift in the paramylon granules that were incubated with the ^{13}C and ^{12}C sources, which were mixed in different ratios, was investigated. The production of the paramylon granules in the cells was induced employing different molar ratios of ^{13}C– and ^{12}C–$NaHCO_3$ (^{13}C: 0, 25, 50, 75, and 100 mol%), after which they were extracted to acquire the Raman spectra and SRS images. The Raman peaks in the CH stretching region gradually shifted toward lower wavenumber positions as the ^{13}C ratio increased (Figure 3a). By plotting the wavenumbers against the ratios of the ^{13}C source in the culture media, a linear relationship was observed (Figure 3b). This result indicates that the ratios of the ^{13}C and ^{12}C constituents of the granules corresponded to those of the carbon sources in the culture media owing to the fixations of $^{13}CO_2$ and $^{12}CO_2$ with equal probabilities, respectively. This result is similar to that of the resonance Raman spectral shifts of carotenoids, which were incubated with a ^{13}C source (ß-carotene and astaxanthin in cyanobacterial[46] and algal cells,[48] respectively). Thereafter, these paramylon granules were visualized via SRS microscopy employing the spectra of 100% ^{13}C– and 100% ^{12}C–paramylon granules (Figure 2a), which were color-coded as red and green, respectively (Figure 3c). Regarding the mixture of 100% ^{13}C– and 100% ^{12}C–paramylon granules, they were discriminated as red and green in the same field of view, respectively. Conversely, the paramylon granules containing ^{13}C and ^{12}C were represented as the gradation colors of red (100% ^{13}C–paramylon granules) and green (100% ^{12}C–paramylon granules) in the RGB color model (e.g., 25%, yellow-green; 50%, yellow; 75%, red-orange; Figure 3c). The histograms of the ratios of ^{13}C in each whole paramylon granule, as calculated by image analysis (Figure S1), reveal that the peaks of the distribution corresponded to the ratios of the ^{13}C sources in the culture media (Figure S2c), because the spectra of the granules containing ^{13}C and ^{12}C were estimated as superpositions of the spectra of 100% ^{13}C– and 100% ^{12}C–paramylon granules at the intensity ratios that corresponded to the incubation ratios (Figure S3), thus generating color codes as the gradation colors. The heatmaps of the ^{13}C ratios in the five segmented regions of the single paramylon granules were uniformly coded with a single gradation color and standard deviations of the average values were relatively low (Figure 3d), indicating that the ^{13}C and ^{12}C constituents were homogeneously distributed in each granule at a constant ratio. These results reveal that the Raman peaks in the CH stretching region were gradually red-shifted linearly as the ^{13}C ratio increased. The ratios of ^{13}C and ^{12}C in the paramylon granules were estimated semi-quantitatively by employing the SRS images of the color-coded spectra of 100% ^{13}C– and 100% ^{12}C–paramylon granules.

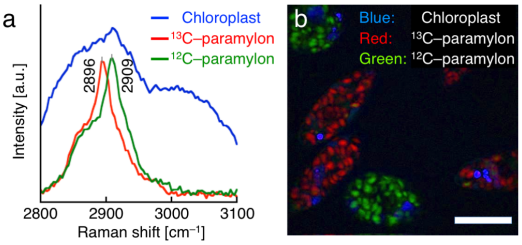

Figure 2. SRS imaging of the mixed *E. gracilis* cells accumulating ^{13}C– or ^{12}C–paramylon granules. (a) Raman spectra of the ^{13}C– and ^{12}C–paramylon granules as well as the chloroplasts in the CH stretching region (2800–3100 cm^{-1}). Red: ^{13}C–paramylon granules, green: ^{12}C–paramylon granules, blue: chloroplasts. (b) An SRS image of the mixed cells. The three constituents (^{13}C– and ^{12}C–paramylon granules, as well as the chloroplasts) are color-coded in red, green, and blue in the RGB color model, respectively. Scale bar: 20 µm.

Time-Resolved SRS Imaging of the Paramylon Granule-Incorporated ^{13}C. Third, the production of paramylon granules in the *E. gracilis* cells was induced using the ^{13}C source, and the incorporation of ^{13}C into the paramylon granules was monitored via SRS imaging. Specifically, the cells were incubated in culture media containing the ^{13}C source for 0, 1, 3, 6, 12, and 24 h (Figure 4a). Next, the ^{13}C constituents in the paramylon granules were investigated by an SRS microscope (Figure 4b). Thereafter, only a few

small-sized ^{12}C–paramylon granules (green) were observed immediately after the induction (0 h, Figure 4b (i)), whereas many large paramylon granules containing the ^{13}C constituent were observed after 3 h of induction, as represented by the gradation colors (yellow or red-orange, Figure 4b (iii)) of red (the ^{13}C constituent) and green (the ^{12}C constituent) in the RGB color model. After 6 h of induction, the amount of the ^{12}C–paramylon granules (green) decreased significantly, and most of the paramylon granules contained the ^{13}C constituent, which was represented as a reddish color (Figure 4b (iv)). After 12 h of induction, most of the paramylon granules contained a high ^{13}C levels (red-orange or red, Figure 4b (v)). The ratio of the ^{13}C constituents of each paramylon granule was calculated by image analysis (Figure S1). The resultant histograms of the ^{13}C ratios reflected the distribution changes that correspond to the results obtained from SRS imaging (Figure 4c). These results indicate that the production of the ^{13}C constituent of the granules proceeded after 3 h of induction; moreover, most of the paramylon granules mainly contained the ^{13}C constituent after 12 h of induction. As demonstrated above, SRS imaging employing the ^{13}C-substrate successfully tracked the production period of paramylon granules.

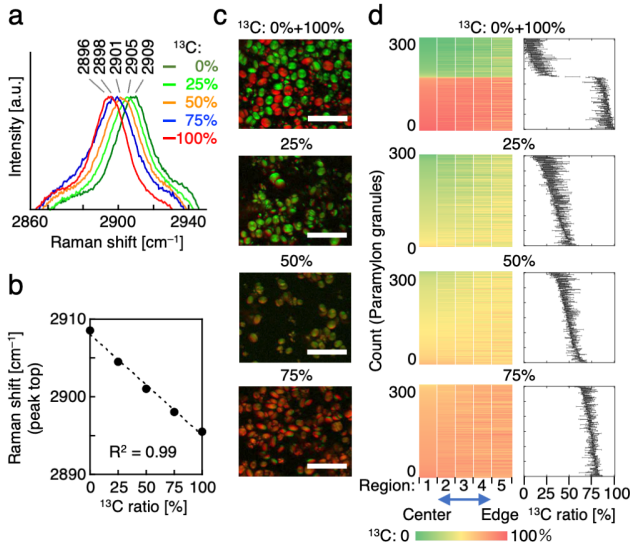

Figure 3. SRS microscopy and statistical analyses of the extracted paramylon granules that were incubated with the ^{13}C and ^{12}C sources in different molar ratios. (a) Enlarged view of the Raman spectra peaks in the CH stretching region of the paramylon granules that were incubated in different ratios of the ^{13}C source. (b) Raman shifts of the peaks against the ratios of the ^{13}C source in the culture media. (c) SRS images of the extracted paramylon granules, which were color-coded as red and green employing the spectra of the 100% ^{13}C– and 100% ^{12}C–paramylon granules, respectively, in the RGB color model. The granules were mixed in the cases of the 0% and 100% ^{13}C sources. Scale bars: 10 µm. (d) Heatmaps (left) and average values with standard deviations (right) of the ^{13}C ratios in the five segmented regions (from the center to the periphery) of the individual paramylon granules (n = 300). The ^{13}C ratios were calculated by analyzing the SRS images (n = 5, including the images in (c)).

SRS Imaging of the Paramylon Granules that were Incubated by Switching the Carbon Source from ^{12}C to ^{13}C. Fourth, the carbon source was switched from ^{12}C to ^{13}C during the production of the paramylon granules, after which the ratios of the ^{12}C and ^{13}C constituents in the paramylon granules were investigated via SRS imaging. Specifically, the time taken to switch from ^{12}C to ^{13}C varied during the 24-hour period of incubation, namely 18, 12, 6, and 3 h, thus extending the later ^{13}C incubation period (Figure 5a). For the control experiments, the cells were incubated with the ^{12}C or ^{13}C source only (Figure 5a (i) and (vi), respectively). The SRS image, as well as the analyzed heatmap and histogram (Figures 5a–c and S5), mainly exhibited the ^{12}C–paramylon granules (green) for the switching at 18 h (condition (ii)). Conversely, regarding the switching at 12 h (condition (iii)), the granules containing the ^{13}C constituent appeared in reddish colors in the image and the heatmap, whereas the histogram of the averaged ^{13}C ratios of the whole granules exhibited the broad distribution (peak: 35%, Figure S5c). Regarding the switching at 6 h (condition (iv)), the greenish (^{12}C-rich) and reddish (^{13}C-rich) granules were observed in a single cell with a markedly broad distribution of the averaged ^{13}C ratios, while the granules with a high ^{13}C constituent (90%–95%) were also observed. Regarding the switching at 3 h (condition (v)), the distribution of the ^{13}C constituent converged to the peak at 90%–95%. These results demonstrate that the ^{13}C ratios of the paramylon granules increased significantly when the cells were incubated with a ^{13}C source in 3–12 h (conditions (iv) and (v)), indicating that the paramylon constituent was actively produced within this period. This finding is consistent with that of time-resolved SRS imaging for the incorporation of ^{13}C into the paramylon granules (Figure 4). The paramylon granules, which were extracted from the cells that were incubated under the same conditions, were also investigated, and the SRS imaging and statistical analyses obtained the same results (Figure S6). Notably, the ^{13}C distribution of the whole paramylon granules in the histograms gradually shifted toward higher values via the intermediate ratios as the ^{13}C incubation time increased, rather than through a bimodal distribution (Figure S5c). Conversely, the greenish (^{12}C-rich) and reddish (^{13}C-rich) colors were observed in the SRS images rather than gradation colors (Figure 5b). Moreover, the standard deviations of the ^{13}C ratios in the five segmented regions of the individual paramylon granules are significantly higher (Figure 5c (iii)–(v)) than those of the paramylons in which ^{13}C and ^{12}C constituents were homogeneously distributed at constant ratios (Figure 3d). These results indicate that the ^{13}C (red) and ^{12}C (green) constituents were heterogeneously localized in a single paramylon granule.

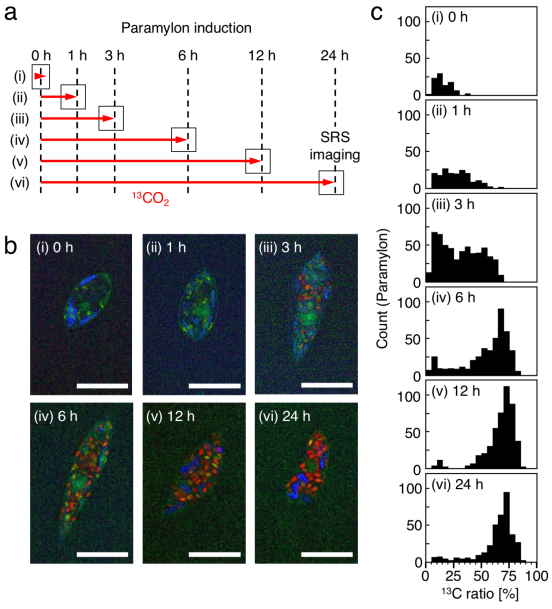

Figure 4. Time-resolved SRS imaging of paramylon granule-incorporated ^{13}C with a ^{13}C source. (a) Timeline of the incubation of the *E. gracilis* cells with ^{13}C incubation. (b) SRS images of the *E. gracilis* cells. The ^{13}C and ^{12}C constituents as well as the chloroplasts were color-coded in red, green, and blue in the RGB color model, respectively, employing the spectra in Figure 2a. Scale bars: 20 µm. (c) Histograms of the ^{13}C ratios of the paramylon granules. The ^{13}C

ratios and counts of the paramylon granules were calculated by analyzing the SRS images (n = 15, including the images in (b)).

To investigate the localization of the ^{13}C constituent under the intermediate conditions, the magnified SRS images of the extracted paramylon granules were investigated (Figures 5d (iii)–(v)). We observed granules in which the ^{13}C constituent was localized around the periphery of the granules, while the ^{12}C constituent was located at the center, as well as ^{13}C-rich and ^{12}C-rich granules. The plots of the ^{13}C ratios in the five segmented regions also supported the localization of ^{13}C constituent around the periphery (Figure 5d, granules B). This result indicates that the newly produced ^{13}C constituent accumulated on the surface of an immature granule since the ^{13}C source was incubated in the later periods. As the later ^{13}C incubation term was extended in the total incubation period (24 h), the ^{13}C constituent infiltrated the granules from the edge toward its center, thus forming a thickened ^{13}C layer (Figure 5d). These differences in the thickness of the ^{13}C layer highlighted the constituent that was accumulated during the incubation periods between the switching times (6 h–12 h (Figures 5a (iii) and (iv)) and 3–6 h (Figures 5a (iv) and (v)), thus reflecting the growing process. This finding emphasizes the benefit of the high-resolution imaging of a single paramylon granule, which revealed the localization of the ^{12}C and ^{13}C constituents, rather than their averaged ratio. As demonstrated above, SRS imaging revealed the active production periods, as well as the growth process of the paramylon granules by switching ^{12}C and ^{13}C incubation at different times, followed by tracing the localization of the ^{13}C constituent in the paramylon granules.

Analysis of the Three-Dimensional SRS Image of a Single Paramylon Granule.

Finally, the localization of the ^{13}C and ^{12}C constituents in a single paramylon granule was investigated via 3D SRS imaging. We scanned the stage position along the depth direction by 0.5 μm steps and acquired a series of SRS images of the immobilized cell, which was incubated under condition (v) in Figure 5a; the images were stacked into a 3D image (Figure 5e). The cross-sectional analysis revealed a paramylon granule with a core–shell structure in which the ^{12}C and ^{13}C constituents acted as the core and shell, respectively, along the XY plane, as well as the XZ and ZY planes (Figure 5f). This core–shell structure was formed by coating the ^{13}C constituent on an immature ^{12}C–paramylon granule, which grew via the $^{12}C/^{13}C$ switching, thus confirming the aforementioned growth process. Additional cross-sectional analyses of the paramylon granules incubated under condition in Figure 5a (iii)–(v) also supported the growth model (Figure S7). As demonstrated above, 3D SRS imaging revealed the localization of the ^{13}C and ^{12}C constituents inside a paramylon granule, thereby elucidating the growth process through which the newly produced constituents were coated on the surface of the immature granule.

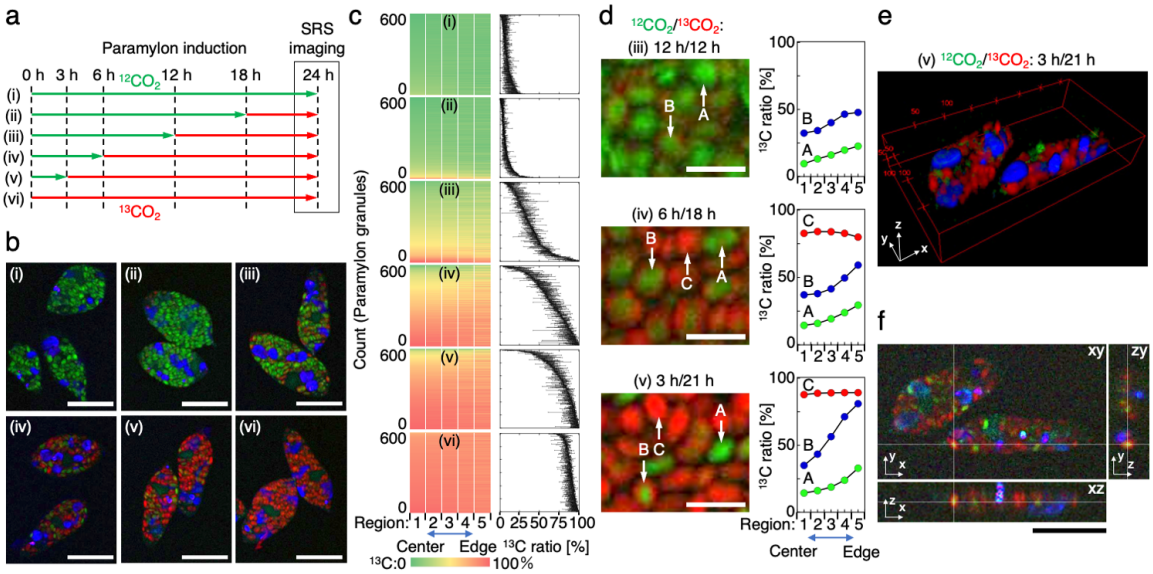

Figure 5. SRS imaging of the *E. gracilis* cells and their paramylon granules that were incubated via atmospheric switching from the ^{12}C to the ^{13}C source. (a) Incubation timeline of the *E. gracilis* cells with incubation switching from the ^{12}C to ^{13}C source at different periods. (b) Representative SRS images of the *E. gracilis* cells that were incubated under the conditions in (a). All the measured SRS images are shown in Figure S4. Scale bars: 20 μm. (c) Heatmaps (left) and average values with standard deviations (right) of the ^{13}C ratios in the five segmented regions (from the center to the periphery) of the individual paramylon granules (n = 600). The ^{13}C ratios were calculated by analyzing the SRS images (n = 9, including the images in (b)). (d) Left: Magnified SRS images of the extracted paramylon granules that were incubated under the conditions in (iii), (iv), and (v) of (a). Representative granules (^{12}C-rich, A; ^{13}C-localized, B; ^{13}C-rich, C) are indicated by arrows. Scale bars: 5 μm. Right: Plots of the ^{13}C ratios of the corresponding granules against the five segmented regions. (e) Three-dimensional SRS imaging of the *E. gracilis* cells that were incubated under the condition in (v) of (a). (f) Cross-sectional analysis of the *E. gracilis* cells in image (e). Scale bars: 20 μm. The ^{13}C and ^{12}C constituents, as well as the chloroplast in all the SRS images, correspond to the red, green, and blue color codes in the RGB color model, respectively, employing the spectra in Figure 2a or Figure S9a.

CONCLUSION

In this study, the spatiotemporal probing of the biogenesis of paramylon granules in *E. gracilis* cells was demonstrated via SRS microscopy in which the $^{13}CO_2$ and $^{12}CO_2$ sources were exposed to different conditions. First, the *E. gracilis* cells, which accumulated the ^{13}C– or ^{12}C–paramylon granules that were produced through carbon fixation, were distinguished via SRS imaging based on the shift in the Raman spectra. Secondly, the red-shift in the Raman spectra of the paramylon granules that were incubated with the ^{13}C and ^{12}C sources, which were mixed in different ratios, was investigated. The Raman peaks gradually red-shifted linearly as the ^{13}C ratio increased, and the ratios of ^{13}C and ^{12}C in the paramylon granules were estimated semi-quantitatively via the SRS imaging of the

color-coded spectra of the two ^{13}C– and ^{12}C–paramylon granules. Third, the incorporation of ^{13}C into paramylon granules was monitored via time-resolved SRS imaging employing the ^{13}C source, which revealed the time taken to produce a paramylon granule. Fourth, the carbon source was switched from ^{12}C to ^{13}C at different times to investigate the ratios of the ^{12}C and ^{13}C constituents of the granules. SRS imaging revealed the active periods, as well as the growth process of the granules by tracing the localization of the ^{13}C constituent of the paramylon granules. Finally, the localization of the ^{12}C and ^{13}C constituents of a paramylon granule was investigated via 3D SRS imaging. The cross-sectional analysis revealed the structures of ^{12}C (core) and ^{13}C (shell), thus confirming the growth process of a paramylon granule accumulating the newly produced constituents on an immature granule.

The method reported herein could be applied to a wide range of organellar activities, including metabolism (degradation and turnover, intracellular trafficking, and extracellular transportation), by detecting the specific Raman spectra. By integrating this method with technologies for single-cell isolation,[45,63] the long-term dynamic processes of storage organelles can be monitored in an identified cell with 3D information. Furthermore, combining with Raman-activated cell sorting[64,65] will enable the screening of the cells which form the target storage organelles (e.g., wax ester in the *E. gracilis* cells) from a large cell population, thus highlighting the unique differences in their metabolic activities. Collectively, our method offers great opportunities for the comprehensive elucidation of the dynamic activities of storage organelles.

ASSOCIATED CONTENT

Supporting Information

The Supporting Information is available free of charge on the ACS Publications website.

Image analysis of ^{13}C ratios; spectral approximation with spectra of ^{13}C and ^{12}C paramylon granules; Additional SRS images of *E. gracilis* cells and paramylon granules; additional Raman spectra of paramylon granules; and plots of pseudo-inverse matrices

AUTHOR INFORMATION

Corresponding Authors

*Yusuke Yonamine
E-mail: yonamine@es.hokudai.ac.jp
*Yasuyuki Ozeki
E-mail: ozeki@ee.t.u-tokyo.ac.jp
*Yu Hoshino
E-mail: yhoshino@chem-eng.kyushu-u.ac.jp

Author Contributions

The manuscript was written through contributions of all authors. All authors have given approval to the final version of the manuscript.

Notes

The authors declare no competing financial interest.

ACKNOWLEDGMENT

This work was funded by the ImPACT program of the Council for Science, Technology, and Innovation (Cabinet Office, Government of Japan).

REFERENCES

(1) Buléon, A.; Colonna, P.; Planchot, V.; Ball, S. Starch Granules: Structure and Biosynthesis. *Int. J. Biol. Macromol.* **1998**, *23*, 85–112.
(2) Ball, S. G.; van de Wal, M. H. B. J.; Visser, R. G. F. Progress in Understanding the Biosynthesis of Amylose. *Trends Plant Sci.* **1998,** *3,* 462–467.
(3) Pérez, S.; Bertoft, E. The Molecular Structures of Starch Components and Their Contribution to the Architecture of Starch Granules: A Comprehensive Review. *Starch-Stärke* **2010,** *62*, 389–420.
(4) Barsanti, L.; Passarelli, V.; Evangelista, V.; Frassanito, A. M.; Gualtieri, P. Chemistry, Physico-Chemistry and Applications Linked to Biological Activities of β-Glucans. *Nat. Prod. Rep.* **2011,** *28*, 457–466.
(5) Monfils, A. K.; Triemer, R. E.; Bellairs, E. F. Characterization of Paramylon Morphological Diversity in Photosynthetic Euglenoids (Euglenales, Euglenophyta). *Phycologia,* **2019,** *50*, 156–169.
(6) Hurlock, A. K.; Roston, R. L.; Wang, K.; Benning, C. Lipid Trafficking in Plant Cells. *Traffic,* **2014,** *15*, 915–932.
(7) Huang, A. H. C. Plant Lipid Droplets and Their Associated Proteins: Potential for Rapid Advances. *Plant Physiol.* **2018,** *176*, 1894–1918.
(8) Weber, E.; Neumann, D. Protein Bodies, Storage Organelles in Plant Seeds. *Biochem. Physiol. Pflanzen,* **1980,** *175*, 279–306.
(9) Schmidt, S. R. Protein Bodies in Nature and Biotechnology. *Mol. Biotechnol.,* **2013,** *54*, 257–268.
(10) Saberianfar, R.; Menassa, R. Protein Bodies: How the ER Deals with High Accumulation of Recombinant Proteins. *Plant Biotechnol. J.,* **2017,** *15*, 671–673.
(11) Jiang, L.; Phillips, T. E.; Hamm, C. A.; Drozdowicz, Y. M.; Rea, P. A.; Maeshima, M.; Rogers, S. W.; Rogers, J. C. The Protein Storage Vacuole: A Unique Compound Organelle. *J. Cell Biol.* **2001,** *155*, 991–1002.
(12) Xiang, L.; Etxeberria, E.; den Ende, W. Vacuolar Protein Sorting Mechanisms in Plants. *FEBS J.,* **2013,** *280*, 979–993.
(13) Thalmann, M.; Santelia, D. Starch as a Determinant of Plant Fitness under Abiotic Stress. *New Phytol.,* **2017,** *214*, 943–951.
(14) Stitt, M.; Zeeman, S. C. Starch Turnover: Pathways, Regulation and Role in Growth. *Curr. Opin. Plant Biol.,* **2012,** *15*, 282–292.
(15) MacNeill, G. J.; Mehrpouyan, S.; Minow, M. A. A.; Patterson, J. A.; Tetlow, I. J.; Emes, M. J.; Raines, C. Starch as a Source, Starch as a Sink: The Bifunctional Role of Starch in Carbon Allocation. *J. Exp. Bot.,* **2017,** *68* , 4433–4453.
(16) Olzmann, J. A.; Carvalho, P. Dynamics and Functions of Lipid Droplets. *Nat. Rev. Mol. Cell Biol.,* **2018,** *20*, 137–155.
(17) Manan, S.; Chen, B.; She, G.; Wan, X.; Zhao, J. Transport and Transcriptional Regulation of Oil Production in Plants. *Crit. Rev. Biotechnol.,* **2016,** *37*, 641–655.
(18) Domergue, J. B.; Abadie, C.; Limami, A.; Way, D.; Tcherkez, G. Seed Quality and Carbon Primary Metabolism. *Plant Cell Environ.,* **2019,** *42*, 2776–2788.
(19) Schenk, P. M.; Thomas-Hall, S. R.; Stephens, E.; Marx, U. C.; Mussgnug, J. H.; Posten, C.; Kruse, O.; Hankamer, B. Second Generation Biofuels: High-Efficiency Microalgae for Biodiesel Production. *Bioenerg. Res.,* **2008,** *1*, 20–43.
(20) Kazamia, E.; Aldridge, D. C.; Smith, A. G. Synthetic Ecology – A Way Forward for Sustainable Algal Biofuel Production? *J. Biotechnol.* **2012,** *162*, 163–169.
(21) Khan, I.; Twyman, R. M.; Arcalis, E.; Stoger, E. Using Storage Organelles for the Accumulation and Encapsulation of Recombinant Proteins. *Biotechnol. J.,* **2012,** *7*, 1099–1108.
(22) Drissi, R.; Dubois, M.-L.; Boisvert, F.-M. Proteomics Methods for Subcellular Proteome Analysis. *FEBS J.,* **2013,** *280*, 5626–5634.
(23) Allen, D. K.; Bates, P. D.; Tjellström, H. Tracking the Metabolic Pulse of Plant Lipid Production with Isotopic Labeling and Flux Analyses: Past, Present and Future. *Prog. Lipid Res.* **2015,** *58*, 97–120.
(24) Niedenführ, S.; Wiechert, W.; Nöh, K. How to Measure Metabolic Fluxes: A Taxonomic Guide for ^{13}C Fluxomics. *Curr. Opin. Biotechnol.* **2015,** *34*, 82–90.
(25) Lichtman, J. W.; Conchello, J. A. Fluorescence Microscopy. *Nat. Methods,* **2005,** *2*, 910-919.
(26) Liu, Z.; Lavis, L. D.; Betzig, E. Imaging Live-Cell Dynamics and Structure at the Single-Molecule Level. *Mol. Cell,* **2015,** *58,* 644–659.
(27) Gautier, A.; Juillerat, A.; Heinis, C.; Correa, I. R., Jr.; Kindermann, M.; Beaufils, F.; Johnsson, K. An Engineered Protein Tag for Multiprotein Labeling in Living Cells. *Chem. Biol.,* **2008,** *15*, 128-136.

(28) Liu, H.-S.; Jan, M.-S.; Chou, C.-K.; Chen, P.-H.; Ke, N.-J. Is Green Fluorescent Protein Toxic to the Living Cells? *Biochem. Biophys. Res. Commun.,* **1999,** *260,* 712–717.
(29) Wang, L.; Frei, M. S.; Salim, A.; Johnsson, K. Small-Molecule Fluorescent Probes for Live-Cell Super-Resolution Microscopy. *J. Am. Chem. Soc.,* **2019,** *141***,** 2770–2781.
(30) Depaoli, M. R.; Bischof, H.; Eroglu, E.; Burgstaller, S.; Ramadani-Muja, J.; Rauter, T.; Schinagl, M.; Waldeck-Weiermair, M.; Hay, J. C.; Graier, W. F.; Malli, R. Live Cell Imaging of Signaling and Metabolic Activities. *Pharmacol. Ther.,* **2019,** *202*, 98-119.
(31) Berry, D.; Mader, E.; Lee, T. K.; Woebken, D.; Wang, Y.; Zhu, D.; Palatinszky, M.; Schintlmeister, A.; Schmid, M. C.; Hanson, B. T.; Shterzer, N.; Mizrahi, I.; Rauch, I.; Decker, T.; Bocklitz, T.; Popp, J.; Gibson, C. M.; Fowler, P. W.; Huang, W. E.; Wagner, M. Tracking Heavy Water (D_2O) Incorporation for Identifying and Sorting Active Microbial Cells. *Proc. Natl. Acad. Sci. U. S. A.,* **2015,** *112,* 194–203.
(32) van Manen, H.-J.; Lenferink, A.; Otto, C. Noninvasive Imaging of Protein Metabolic Labeling in Single Human Cells Using Stable Isotopes and Raman Microscopy. *Anal. Chem.*, **2008,** *80,* 9576–9582.
(33) Wei, L.; Yu, Y.; Shen, Y.; Wang M. C.; Min, W. Vibrational Imaging of Newly Synthesized Proteins in Live Cells by Stimulated Raman Scattering Microscopy. *Proc. Natl. Acad. Sci. U. S. A.*, **2013,** *110,* 11226–11231.
(34) Wei, L.; Shen, Y.; Xu, F.; Hu, F.; Harrington, J. K.; Targoff, K. L.; Min, W. Imaging Complex Protein Metabolism in Live Organisms by Stimulated Raman Scattering Microscopy with Isotope Labeling. *ACS Chem. Biol.,* **2015,** *10***,** 901–908.
(35) Noothalapati Venkata, H. N.; Shigeto, S. Stable Isotope-Labeled Raman Imaging Reveals Dynamic Proteome Localization to Lipid Droplets in Single Fission Yeast Cells. *Chem. Biol.,* **2012,** *19***,** 1373–1380.
(36) Shen, Y.; Xu, F.; Wei, L.; Hu, F.; Min, W. Live-Cell Quantitative Imaging of Proteome Degradation by Stimulated Raman Scattering. *Angew. Chem., Int. Ed.,* **2014,** *53*, 5596–5599.
(37) Wang, Y.; Ji, Y.; Wharfe, E. S.; Meadows, R. S.; March, P.; Goodacre, R.; Xu, J.; Huang, W. E. Raman Activated Cell Ejection for Isolation of Single Cells. *Anal. Chem.,* **2013,** 85, 10697–10701.
(38) Kubryk, P.; Kölschbach, J. S.; Marozava, S.; Lueders, T.; Meckenstock, R. U.; Niessner, R.; Ivleva, N. P. Exploring the Potential of Stable Isotope (Resonance) Raman Microspectroscopy and Surface-Enhanced Raman Scattering for the Analysis of Microorganisms at Single Cell Level. *Anal. Chem.*, **2015,** *87***,** 6622–6630.
(39) Chen, Z.; Paley, D. W.; Wei, L.; Weisman, A. L.; Friesner, R. A.; Nuckolls, C.; Min, W. Multicolor Live-Cell Chemical Imaging by Isotopically Edited Alkyne Vibrational Palette. *J. Am. Chem. Soc.,* **2014,** *136*, 8027-8033.
(40) van Manen, H.-J.; Kraan, Y. M.; Roos, D.; Otto, C. Single-Cell Raman and Fluorescence Microscopy Reveal the Association of Lipid Bodies with Phagosomes in Leukocytes. *Proc. Natl. Acad. Sci. U. S. A.*, **2005,** *102,* 10159–10164.
(41) Zhang, D.; Slipchenko, M. N.; Cheng, J.-X. Highly Sensitive Vibrational Imaging by Femtosecond Pulse Stimulated Raman Loss. *J. Phys. Chem. Lett.,* **2011,** *2,* 1248–1253.
(42) Li, J.; Cheng, J.-X. Direct Visualization of De novo Lipogenesis in Single Living Cells. *Sci. Rep.*, **2014,** *4,* 6807.
(43) Hu, F.; Wei, L.; Zheng, C.; Shen, Y.; Min, W. Live-Cell Vibrational Imaging of Choline Metabolites by Stimulated Raman Scattering Coupled with Isotope-Based Metabolic Labeling. *Analyst,* **2014,** *139,* 2312–2317.
(44) Yonamine, Y.; Suzuki, Y.; Ito, T.; Miura, Y.; Goda, K.; Ozeki, Y.; Hoshino, Y. Monitoring Photosynthetic Activity in Microalgal Cells by Raman Spectroscopy with Deuterium Oxide as a Tracking Probe. *ChemBioChem,* **2017,** *18***,** 2063–2068.
(45) Ota, N.; Yonamine, Y.; Asai, T.; Yalikun, Y.; Ito, T.; Ozeki, Y.; Hoshino, Y.; Tanaka, Y. Isolating Single Euglena gracilis Cells by Glass Microfluidics for Raman Analysis of Paramylon Biogenesis. *Anal. Chem.,* **2019,** *91***,** 9631–9639.
(46) Li, M.; Canniffe, D. P.; Jackson, P. J.; Davison, P. A.; FitzGerald, S.; Dickman, M. J.; Burgess, J. G.; Hunter, C. N.; Huang, W. E. Rapid Resonance Raman Microspectroscopy to Probe Carbon Dioxide Fixation by Single Cells in Microbial Communities. *ISME J.,* **2012,** *6***,** 875–885.
(47) McIlvenna, D.; Huang, W. E.; Davison, P.; Glidle, A.; Cooper, J.; Yin, H. Continuous Cell Sorting in a Flow Based on Single Cell Resonance Raman Spectra. *Lab Chip,* **2016,** *16***,** 1420–1429.
(48) Yonamine, Y.; Hiramatsu, K.; Ideguchi, T.; Ito, T.; Fjiwara, T.; Miura, Y.; Goda, K.; Hoshino, Y. Spatiotemporal Monitoring of Intracellular Metabolic Dynamics by Resonance Raman Microscopy with Isotope Labeling. *RSC Adv.,* **2020,** *10,* 16679–16686.
(49) Koletzko, B.; Sauerwald, T.; Demmelmair, H. Safety of Stable Isotope Use. *Eur. J. Pediatr.,* **1997,** *156,* S12–S17.
(50) Barras, D. R.; Stone, B. A., The Biology of Euglena, Volume II: Biochemistry (Ed.: D. E. Buetow), Academic Press, New York **1968,** p.149–191.
(51) Briand, J.; Calvayrac, R. Paramylon Synthesis in Heterotrophic and Photoheterotrophic Euglena (Euglenophyceae). *J. Phycol.* **1980,** *16,* 234 –239.
(52) Coleman, L. W.; Rosen, B. H.; Schwartzbach, S. D. Environmental Control of Carbohydrate and Lipid Synthesis in *Euglena. Plant Cell Physiol.* **1988,** *29,* 423–432.
(53) Inui, H.; Miyatake, K.; Nakano, Y.; Kitaoka, S. Wax Ester Fermentation in Euglena gracilis. *FEBS Lett.,* **1982,** *150,* 89–93.
(54) Schneider, T.; Betz, A. Waxmonoester Fermentation in Euglena gracilis T. Factors Favouring the Synthesis of Odd-Numbered Fatty Acids and Alcohols. *Planta,* **1985,** *166,* 67–73.
(55) Tucci, S.; Vacula, R.; Krajcovic, J.; Proksch, P.; Martin, W. Variability of Wax Ester Fermentation in Natural and Bleached Euglena gracilis Strains in Response to Oxygen and the Elongase Inhibitor Flufenacet. *J. Eukaryotic Microbiol.,* **2010,** *57,* 63–69.
(56) Rodríguez-Zavala, J. S.; Ortiz-Cruz, M. A.; Mendoza-Hernández, G.; Moreno-Sánchez, R. Increased Synthesis of α-Tocopherol, Paramylon and Tyrosine by Euglena gracilis under Conditions of High Biomass Production. *J. Appl. Microbiol.* **2010,** *109,* 2160–2172.
(57) Ozeki, Y.; Umemura, W.; Otsuka, Y.; Satoh, S.; Hashimoto, H.; Sumimura, K.; Nishizawa, N.; Fukui, K.; Itoh, K. High-Speed Molecular Spectral Imaging of Tissue with Stimulated Raman Scattering. *Nat. Photonics* **2012,** *6,* 844–850.
(58) Wakisaka, Y.; Suzuki, Y.; Iwata, O.; Nakashima, A.; Ito, T.; Hirose, M.; Domon, R.; Sugawara, M.; Tsumura, N.; Watarai, H.; Shimobaba, T.; Suzuki, K.; Goda, K.; Ozeki, Y. Probing the Metabolic Heterogeneity of Live Euglena gracilis with Stimulated Raman Scattering Microscopy. *Nat. Microbiol.* **2016,** *1,* 16124.
(59) Ozeki, Y.; Asai, T.; Shou, J.; Yoshimi, H. Multicolor Stimulated Raman Scattering Microscopy With Fast Wavelength-Tunable Yb Fiber Laser. *IEEE J. Sel. Top. Quantum Electron.* **2019,** *25,* 7100211.
(60) Rasband, W. S., ImageJ, U. S. National Institutes of Health, Bethesda, Maryland, USA, http://imagej.nih.gov/ij/, 1997-2012.
(61) Schneider, C. A.; Rasband, W. S.; Eliceiri, K. W. NIH Image to ImageJ: 25 Years of Image Analysis. *Nat. Methods* **2012,** *9,* 671–675.
(62) Huang, K-C.; Li, J.; Zhang, C.; Tan, Y.; Cheng, J-X. Multiplex Stimulated Raman Scattering Imaging Cytometry Reveals Lipid-Rich Protrusions in Cancer Cells under Stress Condition. *iScience,* **2020,** *23,* Issue 3, 100953.
(63) Vasdekis, A. E.; Stephanopoulos, G. Review of Methods to Probe Single Cell Metabolism and Bioenergetics. *Metab. Eng.,* **2015,** *27*, 115–135.
(64) Hiramatsu, K.; Ideguchi, T.; Yonamine, Y.; Lee, S.; Luo, Y.; Hashimoto, K.; Ito, T.; Hase, M.; Park, J.-W.; Kasai, Y.; Sakuma, S.; Hayakawa, T.; Arai, F.; Hoshino, Y.; Goda, K. High-Throughput Label-Free Molecular Fingerprinting Flow Cytometry. *Sci. Adv.,* **2019,** *5,* eaau0241.
(65) Nitta, N.; Iino, T.; Isozaki, A.; Yamagishi, M.; Kitahama, Y.; Sakuma, S.; Suzuki, Y.; Tezuka, H.; Oikawa, M.; Arai, F.; Asai, T.; Deng, D.; Fukuzawa, H.; Hase, M.; Hasunuma, T.; Hayakawa, T.; Hiraki, K.; Hiramatsu, K.; Hoshino, Y.; Inaba, M.; Inoue, Y.; Ito, T.; Kajikawa, M.; Karakawa, H.; Kasai, Y.; Kato, Y.; Kobayashi, H.; Lei, C.; Matsusaka, S.; Mikami, H.; Nakagawa, A.; Numata, K.; Ota, T.; Sekiya, T.; Shiba, K.; Shirasaki, Y.; Suzuki, N.; Tanaka, S.; Ueno, S.; Watarai, H.; Yamano, T.; Yazawa, M.; Yonamine, Y.; Di Carlo, D.; Hosokawa, Y.; Uemura, S.; Sugimura, T.; Ozeki, Y.; Goda, K. Raman Image-Activated Cell Sorting. *Nat. Commun.*, **2020,** *11,* Article number: 3452.

TOC

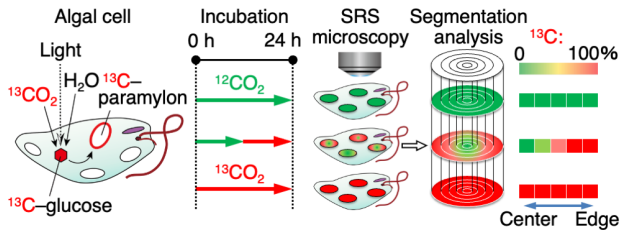
Algal cell
Light
H_2O
^{13}C–paramylon
$^{13}CO_2$
^{13}C–glucose
Incubation
0 h
24 h
$^{12}CO_2$
$^{13}CO_2$
SRS microscopy
Segmentation analysis
^{13}C:
0
100%
Center
Edge